

RSC Advances



This is an *Accepted Manuscript*, which has been through the Royal Society of Chemistry peer review process and has been accepted for publication.

Accepted Manuscripts are published online shortly after acceptance, before technical editing, formatting and proof reading. Using this free service, authors can make their results available to the community, in citable form, before we publish the edited article. This *Accepted Manuscript* will be replaced by the edited, formatted and paginated article as soon as this is available.

You can find more information about *Accepted Manuscripts* in the [Information for Authors](#).

Please note that technical editing may introduce minor changes to the text and/or graphics, which may alter content. The journal's standard [Terms & Conditions](#) and the [Ethical guidelines](#) still apply. In no event shall the Royal Society of Chemistry be held responsible for any errors or omissions in this *Accepted Manuscript* or any consequences arising from the use of any information it contains.

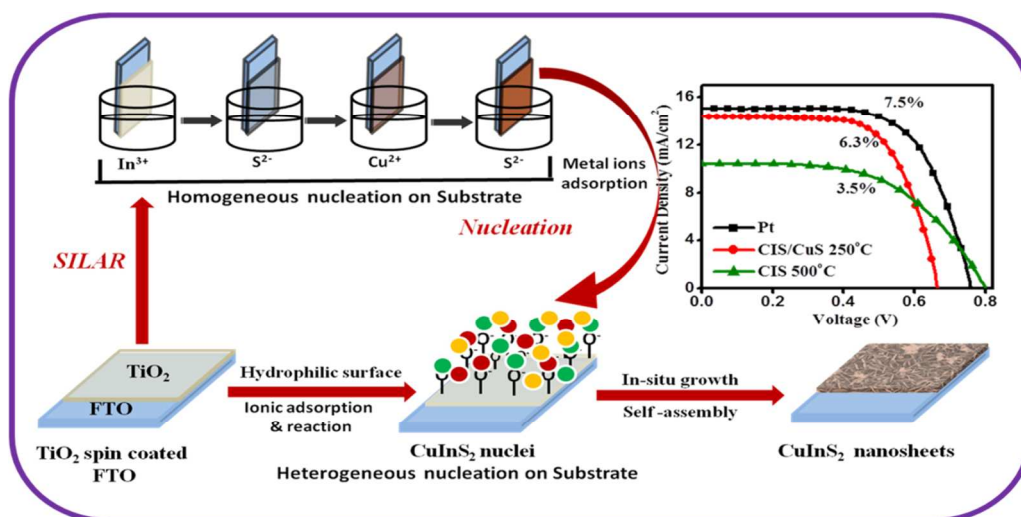
Table of Contents:

Nanophase CuInS₂ nanosheets/CuS composite grown by SILAR method renders high performance as counter electrode in dye sensitized solar cells

Reshma K. Bhosale,^{*a,b,c} Shruti A. Agarkar,^{a,b,c} Ishita Agrawal,^{a,b} Rounak A. Naphade,^{a,b,c} and Satishchandra Ogale^{*a,b,c}

Keywords: Bimetallic sulfide, SILAR, CIS, counter electrode, DSSC

Single phase CuInS₂ (CIS) nanosheets are synthesized on TiO₂ coated FTO by the simple technique of Successive Ionic Layer Adsorption Reaction (SILAR) followed by annealing at 500°C. Annealing at a lower temperature of 250°C is found to yield CuS nanoparticles in addition to the CIS phase. Both the cases of the single phase CIS and the CuS/CIS nanocomposite were examined as counter electrode yielding a power conversion efficiency of 6.3% as compared to pristine CIS (5%) or CuS (3.5%).



Cite this: DOI: 10.1039/c0xx00000x

www.rsc.org/xxxxxx

ARTICLE TYPE

Nanophase CuInS₂ nanosheets/CuS composite grown by SILAR method renders high performance as counter electrode in dye sensitized solar cells[†]

Reshma K. Bhosale,^{*a,b,c} Shruti A. Agarkar,^{a,b,c} Ishita Agrawal,^{a,b} Rounak A. Naphade^{a,b,c} and Satishchandra Ogale^{*a,b,c}

Received (in XXX, XXX) Xth XXXXXXXXX 20XX, Accepted Xth XXXXXXXXX 20XX

DOI: 10.1039/b000000x

Single phase CuInS₂ (CIS) nanosheets are synthesized on TiO₂ coated FTO by the simple technique of Successive Ionic Layer Adsorption Reaction (SILAR) followed by annealing at 500°C. Annealing at a lower temperature of 250°C is found to yield CuS nanoparticles in addition to the CIS phase. Both the cases of the single phase CIS and the CuS/CIS nanocomposite were examined as counter electrode for a dye-sensitized solar cell (DSSC). The CIS/CuS composite is found to render a synergistic effect on catalytic performance toward the reduction of tri-iodide, yielding a power conversion efficiency of 6.3% as compared to pristine CIS (5%) or CuS (3.5%). The possible reasons behind the high performance of the composite case are elucidated using cyclic voltammetry (CV) measurements and electrochemical impedance spectroscopy (EIS).

Introduction

As one of the most promising alternatives for traditional silicon solar cells, dye-sensitized solar cells (DSSCs) have attracted tremendous scientific and industrial attention in the past two decades, owing to their low cost, simple fabrication, and high efficiency.¹ A typical DSSC has a sandwich structure with a photoanode comprising TiO₂ nanoparticles film sensitized by dye molecules, an electrolyte containing the iodide/triiodide (I⁻/I₃⁻) redox couple, and a counter electrode (CE) catalyzing the reduction of I₃⁻ to I⁻. Usually, platinum is the best material for catalyzing the reduction of I₃⁻ due to its superior conductivity, electrocatalytic activity, and stability. However, as a noble metal, low abundance ratio and high cost prevent Pt from being used for DSSCs, which has stimulated great efforts to explore and evaluate substitutes for Pt in order to reduce the overall cost and simultaneously retain the performance of DSSC. Towards this end many alternatives like carbon based material, conducting polymers, and metallic nano-materials have been and are being investigated.²⁻⁵ Transition metal sulfides such as CoS, NiS, SnS appear to be particularly interesting in this context due to their unique catalytic, optical and electrical properties.⁶⁻⁸ Multimetal sulfides too are excellent candidates in photovoltaic applications due to

their direct band gap and high absorption coefficient of more than 10⁵ cm⁻¹. A synergistic mechanism involving various metal elements also renders a higher catalytic activity in such semiconductors. CuInS₂ is one such bi-metallic sulfide which has not yet been fully explored in the DSSC counter electrode context except for a few interesting recent works. For example, Yang et al.⁹ and Liu et al.¹⁰ used hydrothermally and solvothermally synthesized CIS nanosheets and CIS nanoflakes respectively as counter electrode in DSSCs, which exhibited an efficiency of 6%. Composites of CIS have also been explored. For instance Zhang et al.¹¹ reported CIS/PEDOT: PSS composite to increase the adhesion and conductivity of counter electrodes giving an efficiency of 6.5%. Most recently sponge-like CuInS₂ is synthesized by solvothermal method and its composite is made with graphene which gave the power conversion efficiency of 6.18% but only CuInS₂ gave only 3.31% efficiency.¹²

In our work we have synthesized the bimetallic sulfide *in situ* by the facile, well known and easily scalable Successive Ionic Layer Adsorption Reaction (SILAR) method which when used as counter electrode showed an efficiency of 6.3% in DSSC. To the best of our knowledge, this is for the first time any ternary sulfide is synthesized by SILAR as a counter electrode for DSSC. Here

initially grown films were amorphous in nature and when calcined at 500°C yield pure crystalline CuInS₂ nanosheets. These CIS nanosheets when used as counter electrode in DSSC gave an efficiency of 5%. But when calcined below 500°C an efficiency of 6.3% was obtained. Interestingly, our findings based on thorough Raman, X-ray diffraction and multiple characterizations reveal the presence of tiny nanocrystals of CuS, which can defy coarse level characterizations, may in fact be the key to its higher performance as counter electrode material when calcined below 500°C. Thus even when one is claiming a single phase condition based on broad level characterization, the material could be a nano-composite, giving synergistic effect on counter performance. We specifically point out that the two materials are not purposely mixed in any off-stoichiometry ratio but the specific constitution results only from specific controlled thermal annealing.

SILAR is a very simple and inexpensive method to grow semiconductor nanocrystals even for large area applications on various substrates without any special restrictions. Moreover the thickness and composition of the film grown can be controlled easily and accurately by changing the cycle numbers and the immersing processes/sequences. More importantly, since competitive adsorption between different metal ions is caused by a significant difference in solubility products, it is hard to deposit ternary or quaternary metal sulfides in a single solution comprising of two or more cations by the SILAR method. Therefore multiple and sequential (alternate) dippings in solutions of different cations are required. Interestingly this helps in careful control of stoichiometry while at the same time allowing nanophase growth. With this approach we have successfully achieved graphene like 2D layered morphology of metal chalcogenide (CIS) which is an emerging potential material for applications in energy storage (Li ion intercalation), catalysis, photovoltaics etc.

Experimental Section

Synthesis

Before depositing CIS on FTO (F: SnO₂) substrates they are cleaned and spin coated with TiO₂ (Solaronix HT/SC) at 3000 rpm for 60s and annealed at 450°C for 15 mins. Such TiO₂ films were given TiCl₄ treatment by immersing them in TiCl₄ solution at 70°C for 30 mins followed by annealing at 450°C for 30 mins. After this CuInS₂ was deposited by modified SILAR method on TiO₂ coated substrates.¹³ Briefly, the above mentioned substrates were dipped sequentially in aqueous solutions of 0.1 M In₂(Cl)₃ for 60 s, and S ion precursor solution (0.075 M Na₂S, with a pH equal to 11.3 adjusted by a buffer solution of 0.1 M KH₂PO₄ and 0.1 M NaOH) for 150 s. This was followed by dipping in 0.01 M CuCl₂ aqueous solution for 20 s, and again in S ion precursor solution for 150 s. Between each dip, the films were rinsed with de-ionized water for 30 s to remove excess precursors and dried in air before the next dipping. Such an immersion procedure is termed as one cycle for copper indium sulfide deposition, and this immersion cycle was repeated several times (8-20) until the

desired amount of Cu_xIn_yS_z quantum dots (QDs) were incorporated. To increase the crystallinity of SILAR-deposited CuInS₂, samples were annealed at different temperatures (250°C and 500°C) in a split-tube furnace under sulfur atmosphere/ Ar gas for 30 min at a ramp of 2°C/min. CuS is also prepared by SILAR by immersing TiO₂ coated FTO in CuCl₂ (0.1M) and Na₂S (0.1M) for 1min.

Fabrication of the DSSC

A dye-sensitized porous TiO₂ film (12µm) was prepared by loading a TiO₂ slurry layer onto FTO glass by the doctor-blading technique. After calcination at 450°C for 1h, the TiO₂ film was given TiCl₄ treatment followed by immersing in ethanolic solution of ruthenium N719 dye for 24 hrs. This dye-sensitized TiO₂ film is then washed with anhydrous ethanol and finally it was dried in moisture-free air. The dye-sensitized TiO₂ photoanode with an active area of 0.25 cm² and the as-fabricated CE were assembled together. The liquid electrolyte, which is composed of 0.5 M LiI, 0.6 M 1-propyl-2,3-dimethylimidazolium iodide, 0.05 M I₂, and 0.5 M 4-tert-butylpyridine with acetonitrile as the solvent, was then injected between the two electrodes. Platinum counter electrode was prepared by drop casting 50µl H₂PtCl₆ solution on FTO followed by heating at 450°C for 15 mins for comparison purposes.

Characterizations

Phase formation was established by X-ray diffraction (XRD, Philips X' Pert PRO). The Raman spectra were measured with 632 nm laser by a LabRAM HR800 (JY Horiba). Surface morphology of the samples and elemental mapping was studied using field emission scanning electron microscope (FESEM, FEI Quanta 200 3D), High resolution transmission electron microscope (HRTEM, tecnai 300 (T-30)) was applied to investigate the detailed nanostructure of different counter electrodes. The current density-voltage (J-V) characteristics of DSCs were measured under 100mW cm⁻² irradiation (150 W xenon lamp, Oriel Instruments), 1 sun AM 1.5, simulated sunlight (solar simulator) on active area of 0.25 cm². The cyclic voltammetry was measured on the three-electrode system carried out at scan rate of 100mV/s with Ag/AgCl as the reference electrode, Pt foil as the counter electrode and thermally deposited Pt/CIS/CIS-CuS composite as the working electrode. The electrolyte used for this study was 10 mM LiI, 1mM I₂ and 0.1M LiClO₄ in acetonitrile. Electrochemical impedance spectroscopy (EIS) of the CEs was recorded using AUTOLAB PGSTAT 30 and performed on dummy cells with a symmetric sandwich-like structure between two identical electrodes, that is, CE/electrolyte/CE under dark conditions. The CEs used for testing in this paper are for fabricating the DSCs. The frequency range was varied from 105 Hz to 0.01Hz. Thickness of electrodes was measured by surface profiler from Dektak 150, Veeco make.

Results & Discussion

Figure 1 shows the XRD data of as-grown CIS films, films

annealed at 250°C and that annealed at 500°C. The XRD curve in Fig 1(a) is of as-grown CIS films which show no peaks of CIS expect peaks of FTO substrate are seen. This indicates that the as grown CIS films are amorphous in nature. The XRD pattern in Fig. 1(b) refers CIS films annealed at 500°C. It shows peaks at $2\theta = 28.1^\circ$, 46.8° , and 54.5° . When matched with (JCPDS No.85-1575) it confirms that these peaks can be indexed to the (112), (220), and (312) planes of CuInS_2 indicating crystalline pure tetragonal phase.¹⁰ But when the films were annealed at 250°C, Fig.1(c), not only the three main peaks of CIS with slight shift were observed but also occurrence of additional three peaks was noted. These additional three peaks belonged to hexagonal CuS with peak positions at 29.4° , 31.6° , and 48.0° corresponding to the (102), (103), (110) planes. Thus the sample annealed at 250°C showed mixed phase of CIS/ CuS .

The phase equilibria between different components depend on temperature and the formation of the phases is controlled by the kinetics of diffusion of the constituent elements in the intermediate phases. In the present case, sub-phases (such as In_2S_3 , CuIn_5S_8 or CuS) of Cu, In and S occur at the low temperature of 250°C over the experimental reaction time and the temperature is not high enough to overcome diffusive processes. On the other hand, at the elevated temperature of 500°C the diffusive kinetics are accelerated and these sub-phases can react to form single phase CIS over comparable processing time reaching global phase equilibrium at that temperature. Thus, the observed phase formation is a two step process wherein sub-phases form at lower temperature and with further increase in temperature these phases react and form a single phase compound.

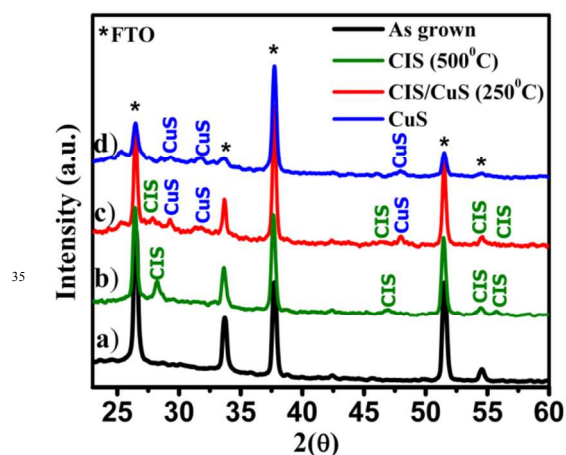


Figure 1: XRD data for (a) As grown copper indium sulfide (CIS) (b) CIS annealed at 500°C (c) CIS annealed at 250°C (d) CuS

Fig.1(d) shows the XRD pattern of pure CuS deposited by the same method. The CuS peaks in this case match well with the CuS peaks in the composite CIS/ CuS annealed at 250°C. Chalcopyrite and sulfide based nanomaterials have very close and similar $2(\theta)$ positions in XRD, hence to have much more clear scenario of phase formation a careful Raman spectroscopy study

is considered essential. CIS has two possible metastable phases, i.e., the Cu–Au (CA)-ordered phase, and the chalcopyrite (CH) phase. Raman spectroscopy is very effective in distinguishing between these two phases. Due to low formation energies, CA-ordered phase and CH phase co-exist at room temperature as stable phase. But, CA-ordered phase is known to be related with decrease of grain size and increase of defects in grains at lower temperature and is unstable at higher temperature.¹⁴⁻¹⁶ In Fig (2) we present the Raman spectra for the sample annealed at 500°C (a) and the one annealed at 250°C (b). For comparison purpose the spectrum for pure CuS sample is also shown (c). Remarkable differences are seen between the cases of samples annealed at the two different temperatures. Most significantly, it is noted that the 250°C annealed sample shows co-existence of CIS and CuS phases, while the one annealed at 500°C shows presence of single phase CIS. This is glaringly brought out by the signature in the domain of $450\text{--}500\text{ cm}^{-1}$; the well-known CuS A_{1g} signature at 472 cm^{-1} .¹⁵⁻¹⁷ Another CuS signature at 263 cm^{-1} is also present in the 250°C annealed sample.

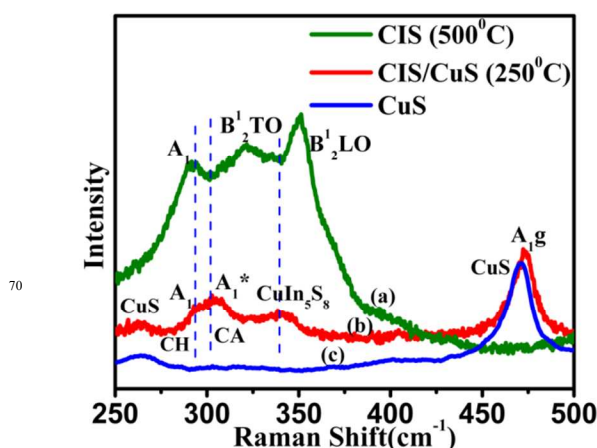


Figure 2: Raman spectra of CIS film (a) annealed at 500°C (b) annealed at 250°C and (c) pure CuS film

In pure CIS (500°C) case A_1 mode of CH phase is clearly observed at 292 cm^{-1} whereas in the case of the composite (250°C) the A_1 mode is broader and split into CH- and CA-ordering which appear at 293 cm^{-1} and 305 cm^{-1} , respectively.^{14,15} It is also to be noted that the full width at half maximum (FWHM) values of the 292 cm^{-1} and 305 cm^{-1} lines are (11 cm^{-1}) and (17 cm^{-1}) than that reported for large single crystal¹⁸ which is very much similar with graphene like samples and this is very well reflected in TEM images shown in Fig.6. Broadening of the Raman bands suggests that the lateral dimensions of these layers are in the nano regime.

The intensity of A_1 mode at 292 cm^{-1} in 250°C case is lower than A_1^* mode due to increase in the Cu/In-ratio. Interestingly, the peak of 305 cm^{-1} from A_1^* mode of CA ordering is dominant in the case of 250°C annealed sample and is totally absent in the pure CIS (500°C annealed case) as it is unstable at higher

temperature. This result implies that the sulfurized metallic film at 500°C is formed with nearly perfect CH ordering of CIS with no secondary phase of Cu₂S and In₂S₃.¹⁵ The 322 cm⁻¹ (B₂¹ TO) and 351 cm⁻¹ (B₂¹ LO) are also from CH ordering.¹⁹ It is reported that β-In₂S₃ shows peaks at 323 cm⁻¹ and 363 cm⁻¹¹⁵ which are not seen in both the cases. But in Indium rich phase, CuIn₅S₈ is indicated by broad signal at around 341 cm⁻¹¹⁶ which co-exists with CIS at 250°C. This CuIn₅S₈ phase is not possible to distinguish in XRD due to very close 2(θ) positions of CIS and CuIn₅S₈ but can be elucidated with higher sensitivity primarily by Raman spectroscopy as shown.²⁰ This peak gets totally vanished in the case of the 500°C annealed sample as CuIn₅S₈ gets chemically transformed into CIS with the help of CuS.^{15,16} Nanoporous film of TiO₂ (thickness 40 nm) used for SILAR is not detected in XRD but is seen in Raman at 148 cm⁻¹ (see in Supporting Information SI).

Morphology

Fig. 3(a, b) shows the images for the film (0.1-1.2 μm) obtained by annealing at 250°C while Fig. 3(c, d) shows the images for the sample annealed at 500°C. These establish that the films comprise of uniform and compact nanosheets which are vertically oriented and interconnected, forming multiple semiconducting channels. In DSSCs, the catalytic reactions take place on the surface of the counter electrodes, thus it is credible that the morphologies of catalytic materials will have an obvious influence on the catalytic reactions. Such a hierarchical architecture not only facilitates transfer of carriers from their surface to the conducting FTO substrate but also endows a large surface area for sufficient light harvesting in optoelectronic applications. We measured the BET surface area for all the three cases although the measurement of BET surface area on thin films is non-trivial. The surface area values for CIS/CuS and CuS were obtained as ~13 m²/g and ~3 m²/g, respectively. The area measured for the single phase CIS case realized at 500°C was below the detection limit of our instrument. This may be due to densification and grain growth which occurs at such high temperature, thereby reducing the surface area significantly.

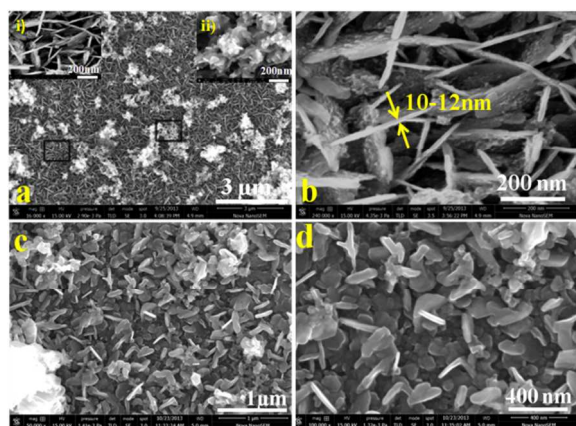


Figure 3: FESEM images of (a) CIS/CuS composite with insets showing two distinct surface features, (b) CIS/CuS thin nanoplates and their typical thickness, (c) and (d) CIS nanosheets under two magnifications.

Separately, we found that as the number of SILAR cycles used was increased from 8 to 20, the thickness of nanosheets increased. Fig. 3(b) represents the case of 16 cycles and the corresponding nanoplate width is seen to be 10-12 nm.

In the composite case (250°C annealed sample), aggregation of CuS nanoparticles (inset ii) is seen to be embedded on CIS nanosheets which is clearly seen in the elemental mapping (Fig. 4(a)) whereas in the 500°C annealed case only CIS nanosheets with no other secondary phase are seen in Fig. 4(b). These nanosheets are fused together due to annealing effect as seen in Fig 3(c, d). Only CuS prepared by SILAR also shows nanoparticle assembly in the form of sea-corals (see in Supporting Information SII). FESEM images of control experiment where CIS is coated directly on FTO without the coating of TiO₂ shows aggregation of irregular particles with random growth (see in supporting information SIII). This clearly indicates that TiO₂ not only facilitates adhesion of film but also give rise to unique morphology of nanosheets by controlling aggregation of particles.

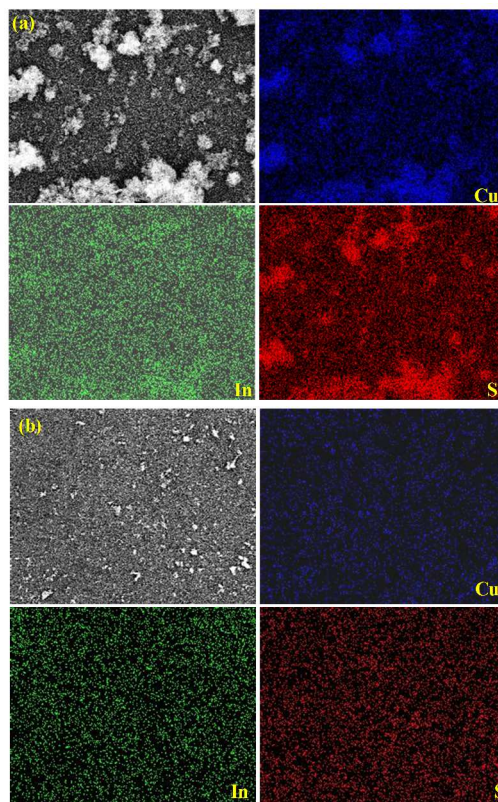


Figure 4: Elemental mapping of (a) CIS/CuS composite, (b) CIS.

The TEM images of the CIS sample annealed at 500°C are shown in Fig. 5(a, b). These reveal graphene like 2D morphology with stacked nanosheets. The bent contour lines in the TEM image are possibly caused either by buckling in the nanosheet introduced in the process of TEM sample preparation or by electron-beam-induced thermal strain during the characterization process. The

lattice spacing of about 0.319 nm can be measured from the HRTEM image which corresponds to the (112) lattice plane spacing of CuInS_2 . The selected area electron diffraction (SAED) pattern confirms that the nanosheet is polycrystalline with planes corresponding to pure CIS. The HRTEM image of the 250°C annealed composite case shown in Fig. 5 reveals that CIS nanosheets (d-spacing 0.31 nm) are decorated with CuS (d-spacing 0.28 nm) nanoparticles of ~5 nm. The SAED pattern gives two sets of signals: One set gives (112) and (312) of CIS whereas the other gives (103) and (110) of CuS.

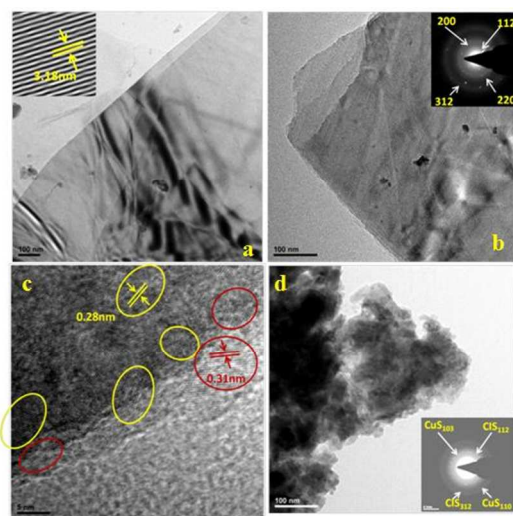


Figure 5: HRTEM images of (a, b) CIS and (c, d) CIS/CuS composite

The proposed mechanism of CIS nanosheets and its composite (Fig 6), on FTO coated TiO_2 is given in detail in supporting information SI VII. Briefly roughness and hydrophilic property of TiO_2 surface provides sites for heterogeneous nucleation.

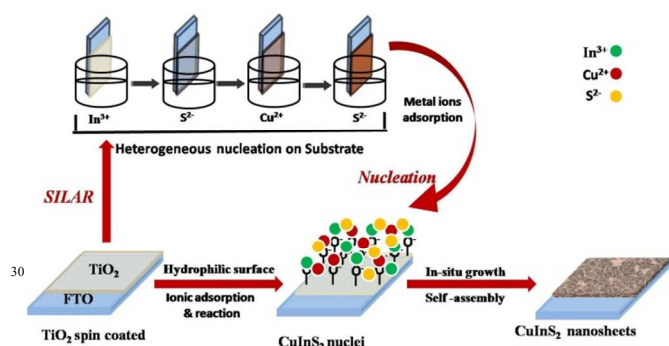


Figure 6: CIS nanosheet formation in SILAR

Further with increase in SILAR cycles, anisotropic growth and self assembly leads to formation of uniform stacked nanosheets. TiO_2 also provides adhesion and coverage of material on FTO. This hierarchical nano structure is strictly dependent on concentration of precursors and dipping time of electrodes in

them. CIS/CuS composite is temperature induced which undergo nucleation–dissolution–recrystallization mechanism.

40 Electrochemical Analysis

For use as counter electrodes in DSSCs these CIS and CIS/CuS composite counter electrodes must show good catalytic activity towards I^-/I_3^- redox reaction. Cyclic voltammetry technique allows qualitative assessment of the electrode kinetics towards this redox couple.²¹ CIS and CIS/CuS composite counter electrodes with different SILAR cycles (8 cycles to 20 cycles) were subjected to cyclic voltammetry analysis. In the case of the counter electrodes, two pairs of redox peaks, I and II, representing sequential redox reactions of different iodide species are seen, corresponding to the reactions



The peak current density helps to evaluate the catalytic activity of the CE, and thus a higher peak current density infers better catalytic activity. The counter electrodes (CEs) fabricated with 16 cycles of both CIS and CIS/CuS composite showed higher current density as compared to other cycles in Fig 7(a) and (b). The peak currents of reduction reactions on different electrodes were noted to follow the order: CIS/CuS > CIS > Pt. Also a shift in the reduction potential towards more negative potential of CIS (-0.28 to -0.38) and CIS/CuS (-0.28 to -0.45), indicates that the oxidized iodide species formed by scavenging photo-excited holes of the dye are easily reduced and regenerated of the electrodes.

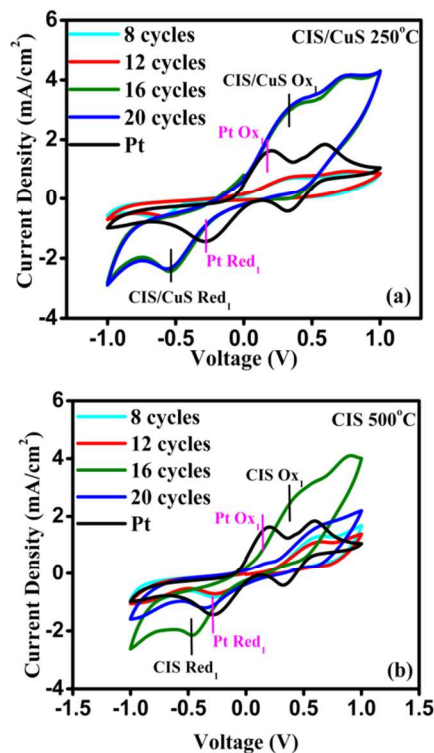


Figure 7: Cyclic Voltammetry data of (a) CIS/CuS composite (b) CIS counter electrodes

Besides this the separation of the anodic and the cathodic peak potentials, peak to peak separation (E_{pp}) of CIS, CIS/CuS and Pt CE was also calculated. The E_{pp} value for Pt counter electrode is 475mV. The E_{pp} is inversely proportional to the catalytic activity of counter electrode towards the redox species. As seen from the figure 7(a) and (b) the E_{pp} is lower for all the cases with CIS/CuS composite as compared to pure CIS. Of all the cycles, for the 16 cycle case, both CIS and CIS/CuS composite counter electrodes show higher current density and lower E_{pp} value indicating better catalytic activity towards I^-/I_3^- reduction. The average E_{pp} for all cases in CIS/CuS composite is 820 mV while it is 870 mV for CIS. Thus the CIS/CuS composite CEs are better towards reduction of iodide-triiodide compared to CIS. CV of pure CuS was also recorded which shows lower performance as compared to CIS and CIS/CuS composite. (See in Supporting Information SI IV)

Photovoltaic Performance

After the cyclic voltametry (CV) analysis, the 16 cycle electrodes of CIS, CIS/CuS composite and CuS were tested as counter electrodes for DSSCs. Figure 8 show the I-V curve for all these cases and Table 1 summarizes the parameters. An efficiency of 6.3% was obtained with the 250°C annealed case of CIS/CuS composite counter electrode while 5% efficiency was obtained with CIS. This is to be compared to 7.5% efficiency obtained with platinum counter electrode. To verify the effect of CuS as counter electrode, 16 SILAR cycles of CuS were deposited on TiO₂ coated FTO and this electrode was also tested as counter electrode in DSSC. This CuS counter electrode gave an efficiency of 3.5% with low current density, open circuit voltage and fill factor as compared to its composite with CIS. Higher current density obtained in the composite case is due to its superior catalytic activity as also seen in the cyclic voltametry analysis. The interconnected nanosheets morphology with CuS on top of it gives good accessibility to the electrolyte with large number of catalytically active sites. The fill factor of this CIS/CuS composite is slightly more than that of Pt which proves that the adhesion (electronic anchoring) and conductivity of this composite is optimal and provides good contact of electrolyte. The only reason for somewhat lower efficiency in the case of composite is its low current density which can be attributed to its relatively weaker catalytic properties as compared to Pt. In the case of pristine CIS the cause for low efficiency may be due to fusion of the CIS nanosheets thus lowering the electrolyte accessible area and thereby the catalytic effectiveness. The low efficiency in case of only CuS counter electrode is of course its poor catalytic activity. Thus the nanocomposite electrode comprising of CIS nanosheets incorporated with CuS renders a synergistic effect as compared with either a pristine CuInS₂ or CuS electrode. All these results confirm that this nano-composite can greatly improve the performance of CE. The cells based on the pristine CuInS₂ counter electrode and temperature induced composite (CIS/CuS) were also studied with respect to different SILAR cycles and their effect on photovoltaic performance (see the supporting information SI V-VI).

55 All the counter electrodes with 8-12 cycles show lower short circuit current density and a lower fill factor compared to 16 cycles. This is probably because the film is too thin to provide enough catalytic sites for I_3^- reduction. With a continued increase in SILAR cycles, the efficiency becomes lower, which can be attributed to higher resistance arising from the thicker CuInS₂ film.

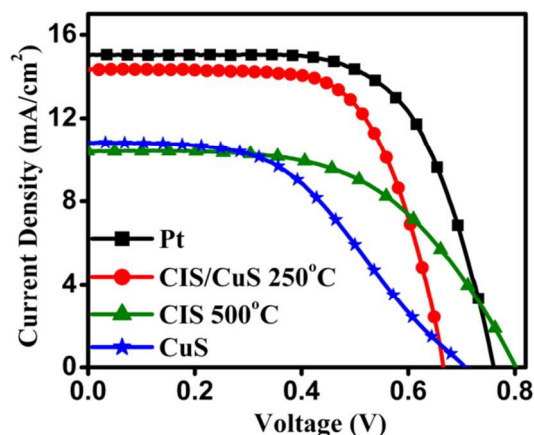


Figure 8: I-V data of counter electrodes with 16 SILAR cycle

Name	V_{oc} (V)	J_{sc} (mA/cm ²)	FF (%)	Efficiency (%)
Pt	0.76	15.04	65.7	7.5
CIS/CuS 250°C	0.67	14.4	66.0	6.3
CIS 500°C	0.8	10.5	55.0	5.0
CuS	0.71	10.8	46.2	3.5

Table 1: I-V parameters of different counter electrode with 16 SILAR cycles

The stability of solar cells with such CIS/CuS based counter electrodes is a concern. As shown in the supporting information (SI VIII), the cell stability is clearly not impressive in this case. However, it was seen to improve with a thin passivation layer of ZnS, also grown by SILAR method. More work on using ALD grown passivation layers which can lead to uniform conformal coatings is needed to push the stability further.

Electrochemical Impedance Analysis

In order to further elucidate catalytic properties of counter electrodes, electrochemical impedance spectroscopy (EIS) analysis was carried out with symmetric cells fabricated with two identical electrodes. In Nyquist plots, the high frequency intercept on the real axis (Z' axis) represents the series resistance R_s while the semicircle region in the high-frequency range is mainly determined by both the charge-transfer resistance R_{ct} and the in parallel capacitance C at the

electrolyte-counter electrode interface. Figure (9) shows the Nyquist plot for pristine CIS, CIS/CuS composite along with the data for Pt counter electrode (inset).

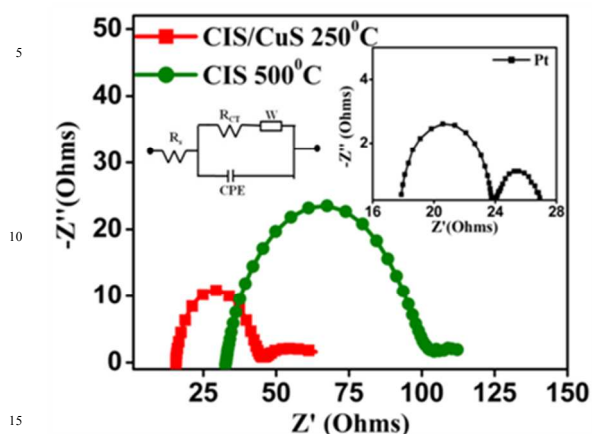


Figure 9: Nyquist plot of counter electrodes with 16 SILAR cycles

The R_{ct} which determines the catalytic activity of the counter electrode is lowest for Pt as seen in the inset. This R_{ct} value is around 29.4 ohms for CIS/CuS composite electrode and 69.2 ohms for pristine CIS counter electrode. R_{ct} is inversely proportional to the catalytic activity of the electrode, thus the CIS/CuS composite electrode is better for catalyzing the I^-/I_3^- redox shuttle. This effect is well reflected in the efficiency data as seen in Figure (8). R_s involves series resistance of FTO, adhesion of counter electrode material on FTO as well as the contact resistance which is higher in case of CIS counter electrode (32 ohms) as compared to CIS/CuS composite case (~15 ohms) as well as Pt. This is due to better conductivity of CIS/CuS composite electrodes as introduction of CuS decreases the series resistance of thin film. Thus it is clear from impedance data as well that CIS/CuS composite is better counter electrode for DSSC. Another technique to analyze the catalytic properties of the counter electrodes is by measurement of Tafel polarization curve.

Fig.10 shows the Tafel plot for Pt, CIS/CuS composite and pristine CIS. These measurements were also carried out in a symmetric cell assembly at a scan rate of 50mV/s. The Tafel curve is usually divided into three regions the lower potential zone is called the polarization zone, the middle region with steep slope is the Tafel zone which determines the catalytic activity of the electrode, and the third zone is the diffusion zone which determines the diffusion of ions in the electrode. In the Tafel zone the intersection of the tangent to the cathodic branch with the equilibrium (zero) potential ordinate is J_0 , which is the exchange current density. The comparison indicates that the CIS/CuS is more effective in catalyzing the reduction of I_3^- than CIS. J_0 is inversely proportional to R_{ct} from the equation:

$$J_0 = RT/nFR_{ct}$$

Where R is constant, T is temperature, n is the number of electrons involved in reaction, and R_{ct} is the charge transfer resistance. A higher J_0 for Pt and CIS/CuS counter electrodes implies a lower value of R_{ct} in the impedance measurement. Another parameter to be extracted from Tafel plot is the limiting current density J_{lim} which describes the diffusion of I_3^- ions in the counter electrode. From the graph it is clear that the diffusion of I_3^- ions in the CIS/CuS composite is higher than that of pristine CIS.

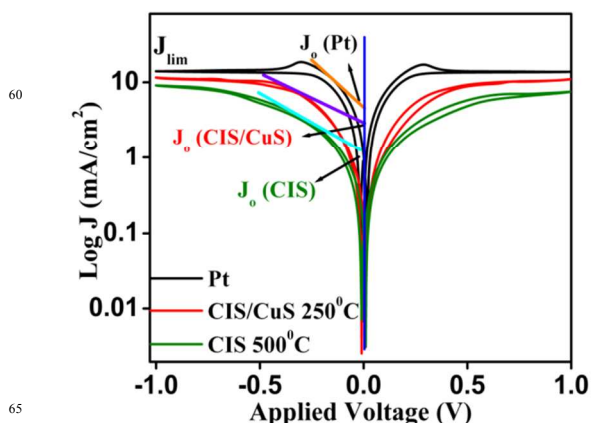


Figure 10: Tafel curve for Pt, CIS/CuS and CIS counter electrodes

To further analyze the diffusion of I_3^- ions in various counter electrodes Randles-Sevcik equation was used.²² Here the anodic peak current values for CIS, CIS/CuS composite and only CuS were recorded at different scan rates to calculate the diffusion coefficients of I_3^- in these electrodes.

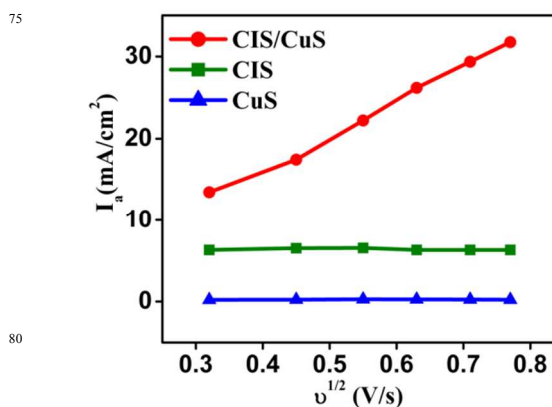


Figure 11: Plot of anodic peak current versus square root of scan rate

Figure 11 shows a linear relationship of anodic peak current density with the square root of scan rate for the cases of interest. These data show that the redox reaction is largely dependent on the diffusion of ions in counter electrode. The diffusion coefficient is directly proportional to the limiting current density as seen from the equation:

$$I_p = K n F A C^*(n F/RT) v^{1/2} D_0^{1/2}$$

where K is the constant (2.69×10^5); A is the area of the electrode; $n = 2$, the number of electrons contributing the charge transfer; F is Faraday's Constant; C^* is the bulk concentration of tri-iodide species. The calculated diffusion coefficients for the three electrodes are CIS ($1.14 \times 10^{-7} \text{ cm}^2 \text{ s}^{-1}$), CIS/CuS ($1.16 \times 10^{-6} \text{ cm}^2 \text{ s}^{-1}$) and only CuS ($1.93 \times 10^{-10} \text{ cm}^2 \text{ s}^{-1}$). This clearly proves that the diffusivity of ions in the CIS/CuS electrode is better as compared to CIS and only CuS. This can be attributed to increased internal porosity due to some CuS segregating on the top surface of the CIS nanosheet film as seen in FESEM images. This leads to an increased contact between the counter electrode material and the electrolyte.

Conclusions

We have synthesized single phase CuInS_2 (CIS) nanosheets on TiO_2 coated FTO by Successive Ionic Layer Adsorption Reaction (SILAR) followed by annealing at 500°C . Annealing at a lower temperature of 250°C yields a morphology comprising of CuS nanoparticles on CIS nanosheets. When examined as counter electrode for dye sensitized solar cell, the CIS/CuS composite is found to render a synergistic effect on catalytic performance toward the reduction of tri-iodide, yielding a power conversion efficiency of 6.3% as compared to pristine CIS (5%) or CuS (3.5%). In addition to various physical property characterizations, the possible reasons behind the higher performance of the nanocomposite are elucidated by employing cyclic voltametry (CV) measurements and electrochemical impedance spectroscopy (EIS).

Notes and references

^aPhysical and Materials Chemistry Division, National Chemical Laboratory, Pune 411008,

^bNetwork Institute of Solar Energy (NISE), New Delhi, India

^cAcademy of Scientific and Innovative Research, Anusandhan Bhawan, 2 Rafi Marg, New Delhi-110001, India

* satishogale@gmail.com, reshmabhosale10@gmail.com

† Electronic Supplementary Information (ESI) available: [Raman spectra of different counter electrodes deposited on TiO_2 coated FTO, FESEM images of TiO_2 layer, CuS electrode, CIS deposited on FTO, CV of CuS, IV of 8-20 SILAR cycles deposited counter electrode, Detailed mechanism, Stability data for the CIS/CuS with and without SILAR-grown ZnS passivation layer.] See DOI: 10.1039/b000000x/

Acknowledgements:

Authors would like to acknowledge Council of Scientific & Industrial Research (CSIR) for financial support. This work was funded by MNRE (TAPSUN) and UK-India APEX (DST). Thanks are due to Abhik Banerjee and Kush Kumar Upadhyay for help with the sulfurization set up. Special thanks to Ms. Dhanya Puthessary, Dr. Sambhaji Warule for help with the electron microscopy images.

References:

1. B. O'Regan, M. Grätzel, *Nature*, 1991, **353**, 737-740.

2. C. Wang, F. Meng, M. Wu, X. Lin, T. Wang, J. Qiu and T. Ma, *Phys. Chem. Chem. Phys.*, 2013, **15**, 14182–14187.
3. R. Gokhale, S. Agarkar, J. Debgupta, D. Shinde, B. Lefez, A. Banerjee, J. Jog, M. More, B. Hannoverc and S. Ogale, *Nanoscale*, 2012, **4**, 6730–6734.
4. L. Bay, K. West, B. Winther-Jensen, T. Jacobsen, *Sol. Energy Mater. Sol. Cells*, 2006, **90**, 341-351.
5. H. Xu, X. Zhang, C. Zhang, Z. Liu, X. Zhou, S. Pang, X. Chen, S. Dong, L. Zhang, P. Han, X. Wang, G. Cui, *ACS Appl. Mater. Interfaces*, 2012, **4**, 1087-1092.
6. G. R. Li, J. Song, G. L. Pan, X. P. Gao, *Energy Environ. Sci.* 2011, **4**, 1680-1683.
7. H. C. Sun, D. Qin, S. Q. Huang, X. Z. Guo, D. M. Li, Y. H. Luo, Q. B. Meng, *Energy Environ. Sci.* 2011, **4**, 2630-2637.
8. X. Chen, Y. Hou, B. Zhang, X. Yang, H. Yang, *Chem. Commun.*, 2013, **49**, 5793-5795.
9. J. Yang, C. Bao, J. Zhang, T. Yu, H. Huang, Y. Wei, H. Gao, G. Fu, J. Liuac, Z. Zouab, *Chem. Commun.*, 2013, **49**, 2028-2030.
10. Y. Liu, Y. Xie, H. Cui, W. Zhao, C. Yang, Y. Wang, F. Huang, N. Daic, *Phys. Chem. Chem. Phys.*, 2013, **15**, 4496-4499.
11. Z. Zhang, X. Zhang, H. Xu, Z. Liu, S. Pang, X. Zhou, S. Dong, X. Chen, G. Cui. *ACS Appl. Mater. Interfaces*, 2012, **4**, 6242-6246.
12. M. Liu, G. Li, X. Chen, *ACS Appl. Mater. Interfaces* 2014, DOI: 10.1021/am405100g.
13. J. Wu, W. Jiang, W. Liao, *Chem. Commun.*, 2010, **46**, 5885-5887.
14. J. Álvarez-García, B. Barcones, A. Pérez-Rodríguez, A. Romano Rodríguez, J. Morante, A. Janotti, S. Wei, R. Scheer, *Phys Rev B*, 2005, **71**, 054303(1-9).
15. D. Lee, J. Kim, *Thin Solid Films.*, 2010, **518**, 6537-6541.
16. E. Rudigier, B. Barcones, I. Luck, J. T. Colin, A. Pe'rez-Rodri'guez, R. Scheer, *J. Appl. Phys.* 2004, **95**, 5153-5158.
17. M. Ishii, K. Shibata, H. Nozaki, *Journal of solid state chemistry*, 1993, **105**, 504-511.
18. H. Matte, A. Gomathi, A. Manna, D. Late, R. Datta, S. Pati, C. Rao, *Angew. Chem. Int. Ed.*, 2010, **49**, 4059-4062.
19. M. Trushin, T. Arguirov, M. Kittler, W. Seifert, A. Klossek, T. Bernhard, W. Gerlach-Blumenthal, A. Tober, M. Schwabe, *Phys. Status Solidi A*, 2013, **210**, 222-225.
20. H. Azimi, T. Heumüller, A. Gerl, G. Matt, P. Kubis, M. Distaso, R. Ahmad, T. Akdas, M. Richter, W. Peukert, C. Brabec, *Adv. Energy Mater.*, 2013, **3**, 1589-1596.
21. R. Crompton, C. Banks, *Understanding Voltametry*, World Scientific Publishing Co. Pte. Ltd: Singapore, 2007.
22. P. Sudhagar, S. Nagarajan, Y. Lee, D. Song, T. Son, W. Cho, M. Heo, K. Lee, J. Won, Y. Kang, *ACS Appl. Mater. Interfaces*, 2011, **3**, 1838-1843.